A 1 cm² Organic Solar Cell with 15.2% Certified Efficiency: Detailed Characterization and Identification of Optimization Potential

Uli Würfel,* Jan Herterich, Mathias List, Jared Faisst, Md Fahmid Matin Bhuyian, Hans-Frieder Schleiermacher, Klara T. Knupfer, and Birger Zimmermann

In organic photovoltaics, high power conversion efficiencies (PCE) are mostly achieved on device areas well below 0.1 cm². Herein, organic solar cells based on a D18:Y6 absorber layer on an active area of ≥ 1 cm² with a certified PCE of 15.24% are reported. The impacts of the sheet resistance of the transparent electrode and the cell design are quantified by means of full optical device simulations and an analytical electrical model. Three imaging methods (light beam-induced current, dark lock-in thermography, and electroluminescence [EL]) are applied and reveal a strong homogeneity of the record cell. Nevertheless, it is found that there is substantial room for improvement mostly in current but also in fill factor and that a PCE of 18.6% on ≥ 1 cm² is feasible with this absorber material. Further, photoluminescence (PL) and EL spectroscopy reveal that both emissions occur at the same wavelength(s) and are very similar to the PL spectrum of a pure Y6 acceptor film. The latter points strongly toward electronic coupling between the S1 states of the acceptor and the charge transfer states at the donor/acceptor interface.

1. Introduction

When reviewing publications in the field of organic photovoltaics (OPV) with high power conversion efficiencies (PCE), one notices that the respective devices' aperture or designated areas are almost always below 0.1 cm², in most cases even below 0.05 cm².[1–11] A recent exception is the work of Cui et al., who, in addition to small spin-coated cells, also report on 1 cm² blade-coated devices with very promising efficiencies, however, not yet certified.[7]

In the research community, record efficiencies of different photovoltaic technologies for measurements under "1 sun" (global AM1.5 spectrum) are listed both in the National Renewable Energy Laboratory (NREL) chart and the solar cell efficiency tables.[12,13] However, the former has no restriction on the actual aperture (or designated) area of the device, the latter requires it to be at least 1 cm² but lists also smaller devices as "notable exceptions." Most importantly, both publications demand that the solar cells must have been independently measured by a recognized test center. The current best values for organic solar cells are 17.5% in the NREL chart (the chart dates however back to September 22, 2020, and information on the device area is not specified), and in the solar cell efficiency tables version 57 (latest when writing this manuscript), it is 15.24% with 1.015 cm² designated area. Further, the efficiency tables list a 0.0322 cm² (designated area) organic solar cell with 18.2% as "notable exception" (which is expected to appear very soon in the NREL chart as well). This demonstrates the significant progress in the field of OPV, as in the previous version 56 of the solar cell efficiency tables, the entries were a device with 1.023 cm² designated area with an efficiency of 13.45% and, as "notable exception," a 0.032 cm² (designated area) organic solar cell with 17.35% efficiency.[14] Furthermore, also on larger areas, the efficiency of organic PV devices could be increased substantially.[15,16]

Our efficiency of 15.24% constitutes 1.79% absolute increase for cells ≥ 1 cm², and we obtained the following key parameters: $J_{SC} = 24.24$ mAcm^{-2}, $V_{OC} = 846.7$ mV, and fill factor (FF) = 74.25%.

Despite this encouraging result, it is striking that there remains a significant gap in comparison with the record efficiencies of very small cells (currently, they are about a factor of 30 smaller). Possible reasons for obtaining lower efficiencies when enlarging the device area are discussed further below.

Dr. U. Würfel, Dr. M. List, J. Faisst, M. F. M. Bhuyian,
H.-F. Schleiermacher, K. T. Knupfer, Dr. B. Zimmermann
Photovoltaics
Organic and Perovskite Photovoltaics
Fraunhofer Institute for Solar Energy Systems ISE
Heidenhofstr. 2, 79110 Freiburg, Germany
E-mail: uli.wuerfel@ise.fraunhofer.de

Dr. U. Würfel, J. Herterich
Freiburg Materials Research Center FMF
Albert-Ludwigs-Universität Freiburg
Stefan-Meier-Str. 21, 79104 Freiburg, Germany

2. Results and Discussion

When increasing the cell size from (far) below 0.1 cm^2 to areas of at least 1 cm^2, there are two main factors which (can) contribute to a decrease in efficiency. The first one is that achieving a highly homogeneous layer (with optimized thickness for light in-coupling and thus current generation) without pinholes or other defects becomes more difficult with increasing area. Every such defect will reduce the current or, even worse, lead in addition to a local shunt which causes losses in fill factor and voltage. The second factor is that a larger cell produces more current and thus the impact of the resistance of the electrodes becomes larger. While the homogeneity of current generation will be analyzed by means of light beam-induced current (LBIC) imaging in more detail, the impact of the finite electrode conductivity can be calculated in a straightforward manner. For this we consider a 1D model where it is important to take the device geometry correctly into account. In the case of a single solar cell, the current flows to more than just one side in contrast to a module with cells interconnected in series. Here, we consider two sides where the current can flow to. Hence, if the shape of the cell is a square, the effective resistance is half of the sheet resistance. Our cell design used for the certified efficiency of 15.24% has a length of 2.2 cm and a width of 0.5 cm. Thus, the transport distance through the transparent electrode (which is indium tin oxide, ITO in our case) underneath the photoactive layer is 0.25 cm and the effective resistance is reduced by a factor of 4.4 compared with a square-shaped cell. Yet another 0.05 cm of transport distance through the ITO has to be added as the metal support structure is placed at this distance from the active region to avoid shunting of the device. As indicated earlier, the latter serves to ensure that the sheet resistance originates (almost) only from the ITO underneath the active area and not from a rather long distance through the ITO to the final contact pad at the edge of the substrate (size is 5 cm × 5 cm).

For sake of simplicity, the (very small) resistances of the metal top contact (Ag, 100 nm thick) and the metal support structure are neglected. Note that the calculations were carried out for a 1 cm^2 cell as the mask used for the certified measurement reduced the area from 1.1 to 1.015 cm^2.

To evaluate the impact of the sheet resistance, we divided the cell into (many) elements and calculated the voltage at each of these elements for a given outer voltage (i.e., the voltage at the contacts). Due to the sheet resistance, each of these elements operates, under current flow, at a (slightly) different voltage. This means that in the fourth quadrant, i.e., positive voltage and negative current, the voltage is larger the farther away the element from the contact. As larger voltage implicates (exponentially) more charge carriers and therefore enhanced recombination, the total current at that specific voltage is reduced compared with the hypothetic case of an infinitely conductive transparent electrode. As a consequence, the fill factor of the solar cell is decreased and with that its efficiency. As the reference device, i.e., a device for which the impact of the resistance of the transparent electrode can be neglected, we chose the 17.6% efficient organic solar cell from the work of Liu et al.[1] This was done for two reasons: first, we have used—at least nominally—the same absorber materials and, second, their device had a very small aperture area of 0.0258 cm^2 only, thus rendering the impact of

the sheet resistance quite insignificant. To enable the use of an analytical model to calculate the efficiency versus sheet resistance of the ITO electrode, we approximated the current–voltage data of their cell by a two-diode model.

$$J(V) = J_{sc} + J_{01}\left(\exp\left[\frac{eV}{k_B T}\right] - 1\right) + J_{02}\left(\exp\left[\frac{eV}{2k_B T}\right] - 1\right) \quad (1)$$

Note that for sake of simplicity, we omitted parallel resistance. The chosen parameters are shown in **Table 1**.

Although the fit is clearly not perfect, it suffices for our purpose here as it reproduces the short-circuit current, the fill factor, and the open-circuit voltage correctly. Next, the current–voltage curve of a 1 cm^2 cell was calculated for different sheet resistances. For this, the voltage at the contacts is set to a certain value and the voltage at the farthest point is guessed (as a starting point). Then, the total current at each position is calculated using the local voltage at that point. The following equations show how this is done for an element i with N being the total number of elements.

$$J_i(V_i) = J_{i-1}(V_{i-1}) + \frac{1}{N}\left(J_{SC} + J_{01}\left(\exp\left[\frac{eV_i}{k_B T}\right] - 1\right)\right.$$
$$\left. + J_{02}\left(\exp\left[\frac{eV_i}{2k_B T}\right] - 1\right)\right) \quad (2)$$
$$V_{i+1} = V_i + J_i(V_i) \times \frac{1}{N} R_s$$

Therein, R_S is the effective resistance of the transparent electrode, i.e., taking the device geometry into account. When "arriving" at V_N (i.e., the voltage at the contact), it is evaluated whether it matches sufficiently accurately with the target value. If not, the starting value V_1 (at the farthest point) is adjusted accordingly in an interval nesting method. This is then repeated for different target voltages to generate the entire new current–voltage curve. There are numerous examples in literature where this or a similar approach has been used to evaluate the impact of a distributed series resistance.[17–21] In this study, the calculations were carried out with Mathematica and the results are shown in **Figure 1**a for different values of the sheet resistance and for two different cell designs. One is simply quadratic and the other corresponds to our design, which was also used for the record cell. As expected, a quadratic-shaped cell is not a smart choice for larger areas as it introduces significant losses already at rather low values of the sheet resistance. In contrast, these losses are strongly reduced for our cell design. Nevertheless, for a transparent electrode with a sheet resistance of 15 Ω, one loses absolute 0.56% efficiency and for 10 Ω, it is still 0.37%. This is due to the rather high current generated by the D18:Y6 absorber. This would suggest to simply use an electrode

Table 1. Parameters used for analytical calculation of the impact of the sheet resistance.

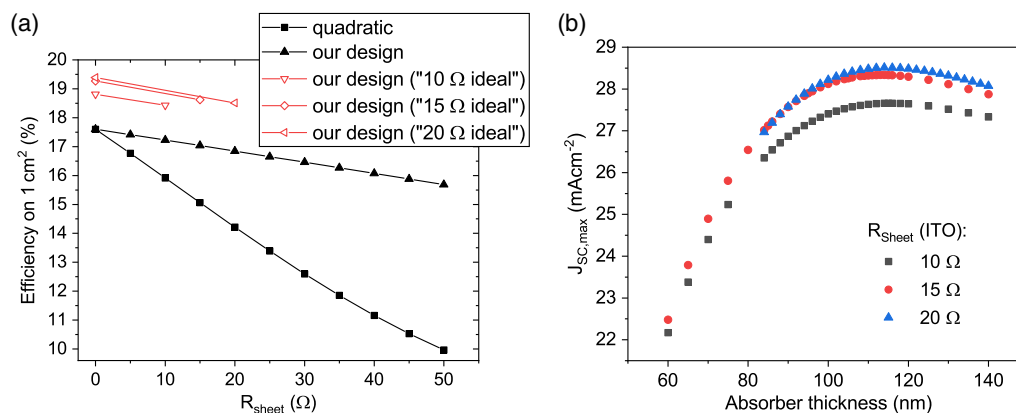| Parameter	Unit	Value
J_{SC}	mA/cm^2	−26.667
J_{01}	mA/cm^2	1.1×10^{-14}
J_{02}	mA/cm^2	1.75×10^{-6}

Figure 1. a) Efficiency as a function of the sheet resistance R_{sheet} of the transparent electrode for a quadratic cell (squares) and for our cell design (triangles). The thin lines are a guide to the eyes. The reference efficiency of 17.6% corresponds to $R_{sheet} = 0$. The hollow symbols are based on the maximum photocurrent resulting from optical simulations shown in (b) (see also text). b) Maximum photocurrent generated in the absorber resulting from full optical device simulations based on n and k values of each layer for ITO electrodes with three different sheet resistances.

with very high conductivity to get rid of these losses or at least significantly reduce them. On the other hand, there is a trade-off between conductivity and transparency, i.e., an ITO with a sheet resistance of 7 or 10 Ω is less transparent than one with 15 Ω due to a thicker ITO layer.

However, the optical properties of the entire device do not scale linearly with the sheet resistance. In fact, the absorption in the photoactive layer of an organic solar cell is strongly influenced by thin-film interference effects, which is why a simple transmission measurement of, e.g., an ITO electrode on glass in air can only serve as a very rough indication. Nevertheless, the transmission curves for the three types of ITO electrodes are shown in Figure S1, Supporting Information. To correctly determine the maximum photocurrent $J_{SC,max}$ generated in the absorber layer, we conducted optical simulations based on the n- and k-values of each layer in the cell stack. The results are shown in Figure 1b for three different sheet resistances of the ITO electrode as a function of absorber thickness. The maximum values are 27.66 mA cm^{-2} for the ITO with a sheet resistance of 10 Ω, 28.34 mAcm^{-2} for 15 Ω, and 28.51 mAcm^{-2} for 20 Ω, respectively.

Next, we evaluated the (electrical) impact of the sheet resistance for these three cases. For this we used the following optimistic but still realistic values of $V_{OC} = 850$ mV and FF = 0.8 to determine how the sheet resistance impacts the performance of near-to-ideal devices (for this particular absorber material). The parameters used for the analytical model are shown in **Table 2**.

For the ITO with 10 Ω, our cell design would result in an efficiency for 1 cm^2 of 18.4%, i.e., a loss of 0.41% absolute. For the case of 15 Ω, the efficiency for 1 cm^2 is reduced to 18.62% which represents a loss of 0.65% absolute. Finally, for a sheet resistance of 20 Ω, the resulting efficiency is reduced by 0.86% absolute to 18.51%. This means that for the D18:Y6 absorber material and our cell design, a sheet resistance of 15 Ω is the best compromise between optical and electrical properties. Note that the optimal absorber thickness in terms of absorption is about 114 nm and depends only weakly on the ITO sheet resistance. Although the absorber layer in our champion device is about 20 nm thinner, this does not constitute a major optical loss as the maximum is rather broad. However, if the electrical properties allow maintaining a high fill factor when increasing the absorber thickness, there is still some room for improvement.

To further evaluate the optimization potential of our 15.24% organic solar cell, we conducted detailed characterization with different imaging techniques. We applied LBIC measurements as well as dark lock-in thermography (DLIT) and electroluminescence (EL). The results are shown in **Figure 2**, with the LBIC image on the left (a) and a histogram of the data on the right (b). For better comparison, the latter was normalized such that the integrated value matches the short-circuit current density J_{SC} of 24.24 mA cm^{-2} that was measured under "1 sun" (global AM1.5 spectrum). It is shown that the current generation is very homogeneous, the distribution is narrow. For example, by omitting all "pixels" lower than the mean value, J_{SC} would increase only by relative 1.6% and the PCE therefore by 0.24% absolute.

Although this does not mean that we achieved an optimal layer thickness in terms of photon absorption in the active layer as discussed above, it either indicates a rather homogeneous coating or reflects the fact that local thickness variations have little impact on the photogenerated current. Although the dependence of the (maximum) generated photocurrent on absorber layer thickness is for this monochromatic illumination more pronounced than for the AM1.5 G spectrum, slight thickness variations do not have a significant impact.
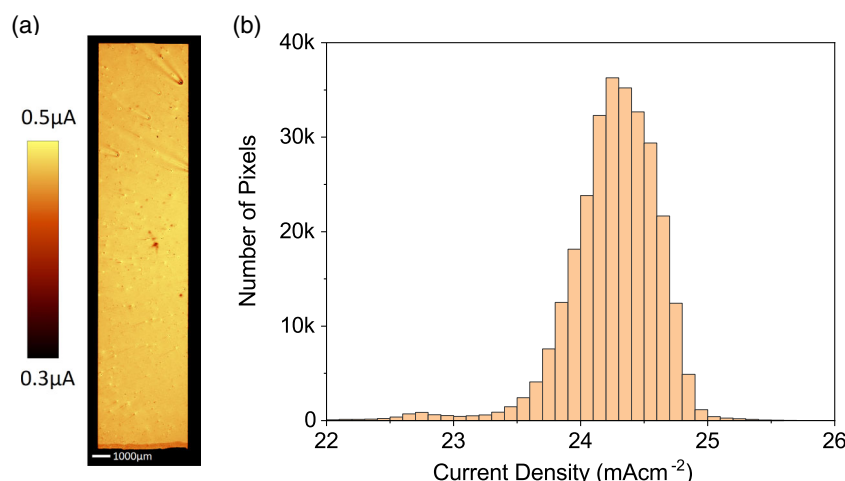
Table 2. Parameters used for analytical calculation of the impact of the sheet resistance with the maximum photocurrent obtained from optical simulations of the complete device stacks.

R_{Sheet} [Ω]	J_{SC} [mA cm^{-2}]	J_{01} [mA cm^{-2}]	J_{02} [mA cm^{-2}]	V_{OC} [mV]	FF	PCE [%]
10	27.66	3.23×10^{-14}	1.16×10^{-6}	850	0.8	18.81
15	28.34	3.3×10^{-14}	1.19×10^{-6}	850	0.8	19.27
20	28.51	3.3×10^{-14}	1.195×10^{-6}	850	0.8	19.39

Figure 2. a) Image of LBIC data of the record 1.1 cm² organic solar cell. b) Histogram showing the distribution of the current density normalized to the value of J_{SC} under "1 sun" (global AM1.5).
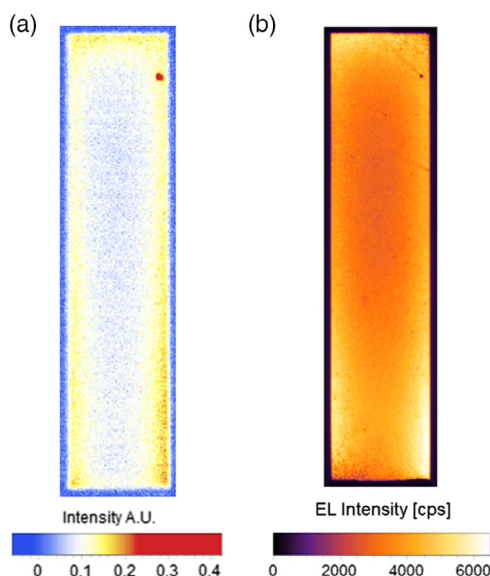

Figure 3. a) Dark lock-in thermography image and b) EL image of the 15.24% device.

Figure 4. PL and EL spectra for a P3HT:PCBM solar cell.

Next, DLIT and EL imaging were conducted; the results are shown **Figure 3**. In the DLIT measurement ((a), left graph), there is one shunt visible in the upper right, but it does not lead to a noticeable V_{OC} reduction (at least not under "1 sun") as compared with other cells that do not have such a clear shunt. The larger signal near the edges is in fact due to the rather large current and hence voltage dropping over the ITO electrode. In the experiment, a voltage of about 1 V was applied and the current was about 70 mA. At such a high current (corresponding to a bit less than $3 \times J_{SC}$ at "1 sun"), the ITO conductivity becomes a limiting factor, causing a considerable gradient in the local voltage and thus current distribution from the edges to the inner area of the cell.

The EL imaging ((b), right side) does also not show any significant inhomogeneity apart from the aforementioned one
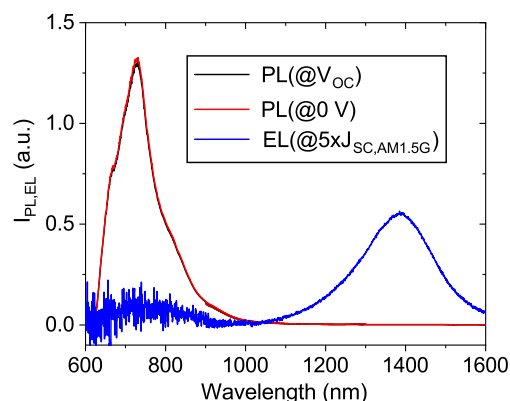
caused by the ITO electrode. Therefore, the three imaging methods showed a very homogeneous cell. However, the optical and electrical modeling presented earlier shows clearly that substantial current losses occur and the fill factor points toward a non-optimal absorber layer morphology.

Finally, we investigated the devices with photo- and electroluminescence (PL and EL) spectroscopy. For comparison, **Figure 4** shows PL and EL spectra for a P3HT:PCBM solar cell. The PL spectra were recorded under illumination of "1 sun" under two different operation conditions (at V_{OC} and at 0 V) and the EL spectrum under a current flow corresponding to $5 \times J_{SC}$ at "1 sun."

It is striking that the PL spectra are extremely dominated by local exciton emission from the P3HT phase and—at least on this scale—no emission from the charge transfer states at the donor/acceptor interfaces can be identified. In contrast, the EL spectrum is dominated by the charge transfer (CT) emission, which has its peak at much longer wavelengths due to a rather large offset between the lowest unoccupied molecular orbital levels of the donor and acceptor beyond 0.5 eV. Although the number of recombining charge carriers is comparable for the PL

measurement under open-circuit conditions and the EL experiment, the peak emission intensity is roughly four orders of magnitude smaller for the EL data. This shows clearly that (local) excitons in the P3HT phase have a significantly larger probability for radiative recombination than (free) charge carriers recombining via the interfacial CT states. Further, the PL signal at 0 V is even slightly larger than the one at V_{OC}. This can be explained by the fact that the probability for a nonradiative decay of excitons in the P3HT increases with increasing charge carrier density.[22–27] But more important here is the fact that the PL signal is not suited to directly derive any reliable information on the recombination of free charge carriers in the absorber. Although Spies et al. have shown how to extract information about the densities of free charge carriers from a differential PL signal,[28] this is far more complicated than in the case of inorganic solar cells where a direct relation between the PL intensity and the charge carrier density can be used to determine multiple quantities such as, e.g., the lifetime of minority carriers, their diffusion length, as well as doping densities and even the quality of charge extraction layers.[29–37]

For our very efficient devices based on D18:Y6, the energy levels (in this case the HOMO levels) of the donor and acceptor are very close together.[1] **Figure 5** shows, for a D18:Y6 solar cell with the aforementioned device stack, the PL spectra (under "1 sun" illumination and different bias voltages) as well as the EL spectrum at an injected current corresponding to the device's J_{SC} under "1 sun."

Comparing these results with the solar cell with a P3HT:PCBM absorber layer, three major differences become obvious: first, the PL and EL spectra are very similar with regard to their wavelength dependence; second, the EL intensity is (again, for roughly equal recombination currents) now not anymore orders of magnitude lower than the PL intensity but only about a factor of 7; and third, the PL intensity now increases with increasing applied voltage. The latter can also nicely be seen from the ΔPL signal, i.e., the difference of the PL at V_{OC} and at 0 V (purple curve).

However, it is still not possible to derive direct information about the charge carrier densities as the signal is still dominated by a contribution that is not (or at least not directly) related to the concentration of electrons and holes. This can be deduced from the fact that the PL intensity at an applied voltage of −2 V is still about 80% of its value at V_{OC}. Note that the PL intensity is not
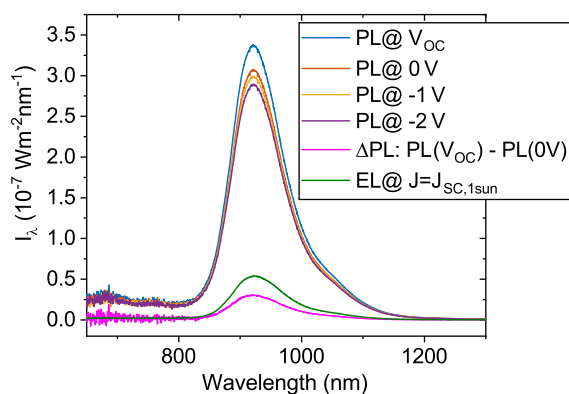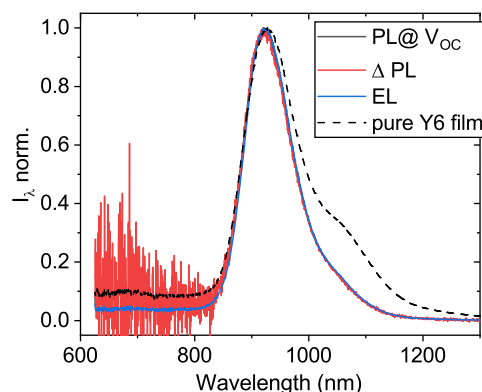

Figure 6. Normalized PL and EL spectra of a D18:Y6 solar cell, together with the PL of a pure Y6 film on glass.

determined exclusively by the external voltage but by the internal quasi Fermi-level separation in the absorber. In fact, the latter can differ from the external voltage due to transport-related voltage drops (i.e., gradients of the quasi-Fermi levels required as driving forces for the transport of charge carriers).[38] However, the investigated D18:Y6 solar cell is very efficient and has a decent fill factor; hence, there should only be a very low concentration of electrons and holes present at an applied negative voltage. This leads to the conclusion that the PL signal originates mainly from local excitons.

To better compare the wavelength dependence of the emission, **Figure 6** shows selected normalized spectra of PL and EL from Figure 5, together with the PL of a pure Y6 acceptor film on glass.

The similarity of the spectra is striking. This points strongly toward a hybridization between excited CT states and the S1 states of the Y6 acceptor—an effect which is also referred to as intensity borrowing and was described recently in the context of organic solar cells by Eisner et al.[39,40] Due to hybridization, the emission probability for electrons and holes recombining at the donor/acceptor interfaces increases. This facilitates the detection of the radiative recombination of electron–hole pairs—in fact the PL and EL intensity from a D18:Y6 device is much larger than the one from a P3HT:PCBM solar cell. However, this does not automatically mean that the hybridization leads to an increased voltage and therefore efficiency. Moreover, hybridization makes it impossible to distinguish between the radiative recombination of local excitons (here: in the acceptor phase) and the one of (free) electrons and holes under operating conditions. For this reason, although the PCEs of these organic solar cells are very promising, no direct information about the actual charge carrier densities can be derived from the measurement of the PL intensity—in contrast to inorganic solar cells where this is frequently done.

3. Conclusion

We have fabricated organic solar cells with D18:Y6 as the absorber materials and achieved a certified efficiency of 15.24% on a designated area ≥1 cm². This constitutes an

Figure 5. PL (under "1 sun", at different bias voltages) and EL spectra for a D18:Y6 device.

absolute increase of 1.79% in this category and reduces the efficiency gap to very small cells. The impact of the optical and electrical properties of the transparent electrode on device performance upon enlarging the cell area was analyzed quantitatively. For optimized photocurrent generation with a $15\,\Omega$ ITO electrode and optimistic (yet realistic) assumptions for the open-circuit voltage and fill factor, an efficiency of 18.6% seems to be achievable on $1\,cm^2$ with the absorber material D18:Y6 used in this study.

Different imaging methods were applied to elucidate the homogeneity of the device which was found to be high. Nevertheless, optical simulations of the complete device stack revealed that the record cell still suffers from considerable current losses of roughly $4\,mAcm^{-2}$. Further optimization potential therefore includes the adjustment of film thickness for improved light incoupling and thus current generation and an increase of the fill factor by improving the morphology in the absorber layer.

PL and EL spectroscopy revealed hybridization between local excitonic S1 states in the acceptor phase and excited CT states at donor/acceptor interfaces. Although luminescence emission is rather strong in these devices, no direct correlation between PL intensity and the density of electrons and holes is obtained.

The recent advancements in OPV are very encouraging. OPVs' undoubtful advantages of low weight and mechanical flexibility, integrability, and potential semitransparency have been repeated almost like a mantra. However, further serious obstacles have to be overcome in order for OPVs to become a viable technological solution. These are primarily further significant increase in efficiency especially on larger areas and substantial improvements of long-term stability. That a high efficiency strongly matters can be seen from the market-dominating crystalline silicon PV technology where the module costs are "only" 40% of the total costs of a PV installation.[41] Although OPVs might, e.g., require less-demanding mounting structures, the balance of system costs will nevertheless constitute a "pressure" toward high efficiencies.

Many innovative synthetic approaches to create numerous novel organic absorber materials and new insights into morphology stabilization through the use of more than two components in the photoactive layer are promising pathways to reach these goals.

4. Experimental Section

Device Fabrication: The solar cells were fabricated using the following device stack

$$Glass/ITO/PEDOT:PSS\,(40\,nm)/D18:Y6\,(90\,nm)/ \qquad (3)$$
$$PDIN\,(5\,nm)/Ag\,(100\,nm)$$

The ITO glasses (Visiontek Systems LTD, 15 Ohm) were sonicated twice in acetone, twice in isopropanol, and finally in deionized water for 10 min each. Then, a current collecting layer (support structure) of Cr (5 nm)/Au (100 nm) was evaporated on both sides and at a distance of 0.5 cm from the active layer. This was done to enhance the conductivity of the ITO electrode, thus ensuring that the sheet resistance originates (almost) only from the ITO underneath the active layer as the substrate size was rather large (5 cm × 5 cm). Prior to the liquid coatings, the substrates were treated under UV–ozone for 20 min. PEDOT:PSS (Ai4083 from Heraeus) filtered through a 0.45 μm syringe filter was spin coated as the hole transport layer at 3000 rpm in air for 60 s and annealed at 130 °C for 10 min after transfer into a nitrogen-filled glovebox.

Subsequently, the absorber material D18:Y6 (1-Material, used as received; molecular weight [GPC]: ≈105 000; PDI ≈2.5) in a ratio of 1:1.6 was spin coated from chloroform solution with a total concentration of $11\,mg\,ml^{-1}$ at 2000 rpm for 30 s. The solution was stirred overnight at room temperature. Instead of solvent annealing, thermal annealing at 100 °C for 10 min was applied. PDIN (1-Material, used as received) electron transport layer was spin coated from methanol with a concentration of $2\,mg\,mL^{-1}$ with 0.27 vol% acetic acid (p.a. grade from Sigma Aldrich) stirred overnight at room temperature. The layer was spin coated at 5000 rpm for 30 s. The top electrode was formed by 100 nm of Ag deposited by thermal evaporation in ultra-high vacuum. Finally, the cells were encapsulated using an adhesive tape (3M 91 022) as pre-encapsulation plus an overlapping glass using DELO LP 655 UV–curing epoxy as the seal.

Optical Simulations: Transmission and reflection spectra of both the ITO electrodes and absorber blend films on plain glass substrates were measured with a Perkin Elmer Lambda 900 UV–vis–spectrometer. The spectra of the bare electrodes are shown in Figure S1, Supporting Information. The 15 and $20\,\Omega$ ITO glasses were purchased from Visiontek Systems LTD, whereas the $10\,\Omega$ ITO was purchased from Kintec, Hongkong. Layer thicknesses were determined with a Veeco Dektak 150 profilometer. The software SCOUT (mtheiss.com) was used to fit the spectra and thus obtain the complex refractive indices of used materials. To calculate the maximum current, assuming that each photon absorbed in the active layer yields one electron–hole pair, the whole layer stack of the cell was simulated as a thin-film interference system by a rigorous-coupled wave analysis algorithm.[42–44]

LBIC Measurement: A commercially available confocal Raman scanning microscope (Witec) was used to focus a laser beam onto the sample (laser spot full width half maximum: ≈ 5 μm). With a low noise current amplifier, the current output of the cell was measured at each scanning position every 20 μm. The laser used for excitation was a 635 nm diode laser (2 μW from Laserpower).

DLIT Measurement: The setup used for DLIT characterization was a custom-made tool by the company IRCAM GmbH. The camera contained an InSb-based mid-wave infrared focal plane array (MWIR FPA) detector, sensitive to IR radiation in the range of 1.5–5 μm, and was actively cooled, resulting in low thermal noise and a temperature resolution limit of < 20 mK. The solar cell was subjected to a periodical bias voltage of a Toellner four-quadrant power supply and the IR camera signal was analyzed using a lock-in amplifier to further increase the signal-to-noise ratio.

EL Imaging: EL imaging was realized by the use of an actively cooled silicon CCD camera (1024 × 1024 pixels). The bias voltage was adjusted with a Keithley 2400 source meter to comparable values used for DLIT characterization.

EL and PL Spectroscopy: A detailed description of the used setup can be found in the work of List et al.[45] The shown EL and PL intensities are not absolute numbers. However, the measured spectra have the same relative unit proportional to $W\,m^{-2}\,nm^{-1}$ and can therefore be compared among each other. Samples were produced, stored, and measured in an inert nitrogen atmosphere. For the PL measurements, the intensity of the cw-Nd:YAG laser ($\lambda_{exc.}$ = 532 nm) was adjusted to generate the same short-circuit current density as the cells had under the sun simulator (simulated AM1.5 G). EL spectra were measured at a corresponding forward current density $J_{EL} = J_{SC}$(AM1.5 G). The width of the entrance slit of the spectrograph was 2 mm for $P3HT:PC_{61}BM$ and 0.5 mm for D18:Y6.

Supporting Information

Supporting Information is available from the Wiley Online Library or from the author.

Acknowledgements

Conflict of Interest

The authors declare no conflict of interest.

Data Availability Statement

Research data are not shared.

Keywords

[1] Q. Liu, Y. Jiang, K. Jin, J. Qin, J. Xu, W. Li, J. Xiong, J. Liu, Z. Xiao, K. Sun, S. Yang, X. Zhang, L. Ding, *Sci. Bull.* **2020**, *65*, 272.

[2] L. Arunagiri, Z. Peng, X. Zou, H. Yu, G. Zhang, Z. Wang, J. Y. Lin Lai, J. Zhang, Y. Zheng, C. Cui, F. Huang, Y. Zou, K. S. Wong, P. C.Y. Chow, H. Ade, H. Yan, *Joule* **2020**, *4*, 1790.

[3] L. Meng, Y. Zhang, X. Wan, C. Li, X. Zhang, Y. Wang, X. Ke, Z. Xiao, L. Ding, R. Xia, H.-L. Yip, Y. Cao, Y. Chen, *Science* **2018**, *361*, 1094.

[4] T. Yan, W. Song, J. Huang, R. Peng, L. Huang, Z. Ge, *Adv. Mat.* **2019**, *31*, 1902210.

[5] Y. Lin, B. Adilbekova, Y. Firdaus, E. Yengel, H. Faber, M. Sajjad, X. Zheng, E. Yarali, A. Seitkhan, O. M. Bakr, A. El-Labban, U. Schwingenschlögl, V. Tung, I. McCulloch, F. Laquai, T. D. Anthopoulos, *Adv. Mat.* **2019**, *31*, 1902965.

[6] J. Song, C. Li, L. Zhu, J. Guo, J. Xu, X. Zhang, K. Weng, K. Zhang, J. Min, X. Hao, Y. Zhang, F. Liu, Y. Sun, *Adv. Mat.* **2019**, *31*, 1905645.

[7] Y. Cui, H. Yao, J. Zhang, K. Xian, T. Zhang, L. Hong, Y. Wang, Y. Xu, K. Ma, C. An, C. He, Z. Wei, F. Gao, J. Hou, *Adv. Mat.* **2020**, *32*, 1908205.

[8] W. Zhang, J. Huang, J. Xu, M. Han, D. Su, N. Wu, C. Zhang, A. Xu, C. Zhan, *Adv. Energy Mater.* **2020**, *10*, 2001436.

[9] L. Zhan, S. Li, T.-K. Lau, Y. Cui, X. Lu, M. Shi, C.-Z. Li, H. Li, J. Hou, H. Chen, *Energy Environ. Sci.* **2020**, *13*, 635.

[10] C. Zhu, J. Yuan, F. Cai, L. Meng, H. Zhang, H. Chen, J. Li, B. Qiu, H. Peng, S. Chen, Y. Hu, C. Yang, F. Gao, Y. Zou, Y. Li, *Energy Environ. Sci.* **2020**, *13*, 2459.

[11] D. Li, X. Chen, J. Cai, W. Li, M. Chen, Y. Mao, B. Du, J. A. Smith, R. C. Kilbride, M. E. O'Kane, X. Zhang, Y. Zhuang, P. Wang, H. Wang, D. Liu, R. A. L. Jones, D. G. Lidzey, T. Wang, *Sci. China Chem.* **2020**, *63*, 1461.

[12] NREL, Best Research-Cell Efficiency Chart, https://www.nrel.gov/pv/cell-efficiency.html (accessed: December 2020).

[13] M. Green, E. Dunlop, J. Hohl-Ebinger, M. Yoshita, N. Kopidakis, X. Hao, *Prog. Photovolt. Res. Appl.* **2021**, *29*, 3.

[14] M. A. Green, E. D. Dunlop, J. Hohl-Ebinger, M. Yoshita, N. Kopidakis, X. Hao, *Prog. Photovolt. Res. Appl.* **2020**, *28*, 629.

[15] A. Distler, C. J. Brabec, H.-J. Egelhaaf, *Prog. Photovolt. Res. Appl.* **2021**, *29*, 24.

[16] S. Dong, T. Jia, K. Zhang, J. Jing, F. Huang, *Joule* **2020**, *4*, 2004.

[17] P. Kopola, B. Zimmermann, A. Filipovic, H.-F. Schleiermacher, J. Greulich, S. Rousu, J. Hast, R. Myllylä, U. Würfel, *Sol. Energy Mater. Sol. Cells* **2012**, *107*, 252.

[18] Y. Galagan, B. Zimmermann, E. W.C. Coenen, M. Jørgensen, D. M. Tanenbaum, F. C. Krebs, H. Gorter, S. Sabik, L. H. Slooff, S. C. Veenstra, J. M. Kroon, R. Andriessen, *Adv. Energy Mater.* **2012**, *2*, 103.

[19] M. Niggemann, B. Zimmermann, J. Haschke, M. Glatthaar, A. Gombert, *Thin Solid Films* **2008**, *516*, 7181.

[20] M. Seeland, H. Hoppe, *Phys. Status Solidi A* **2015**, *212*, 1991.

[21] M. Burgelman, A. Niemegeers, *Sol. Energy Mater. Sol. Cells* **1998**, *51*, 129.

[22] N. H. Hansen, C. Wunderlich, A. K. Topczak, E. Rohwer, H. Schwoerer, J. Pflaum, *Phys. Rev. B* **2013**, *87*.

[23] J. C. Bolinger, M. C. Traub, T. Adachi, P. F. Barbara, *Science* **2011**, *331*, 565.

[24] I. Rörich, Q. Niu, B. der Zee, E. del Pino Rosendo, N. I. Crăciun, C. Ramanan, P. W. M. Blom, *Adv. Electron. Mater.* **2020**, *6*, 1700643.

[25] D. Banerjee, A. K. Kar, *Phys. Chem. Chem. Phys.* **2018**, *20*, 23055.

[26] Y. Luo, H. Aziz, G. Xu, Z. D. Popovic, *Chem. Mater.* **2007**, *19*, 2288.

[27] J. S. Bangsund, J. R. Van Sambeek, N. M. Concannon, R. J. Holmes, *Sci. Adv.* **2020**, *6*, eabb2659.

[28] A. Spies, M. List, T. Sarkar, U. Würfel, *Adv. Energy Mater.* **2017**, *7*, 1601750.

[29] T. Trupke, R. A. Bardos, M. C. Schubert, W. Warta, *Appl. Phys. Lett.* **2006**, *89*, 44107.

[30] B. Hallam, B. Tjahjono, T. Trupke, S. Wenham, *J. Appl. Phys.* **2014**, *115*, 44901.

[31] J. A. Giesecke, M. C. Schubert, B. Michl, F. Schindler, W. Warta, *Sol. Energy Mater. Sol. Cells* **2011**, *95*, 1011.

[32] F. D. Heinz, P. Gundel, W. Warta, M. C. Schubert, *IEEE J. Photovolt.* **2013**, *3*, 341.

[33] T. Enkhbat, M. S. Mina, M. H. Sharif, E. Enkhbayar, K. Y. Jung, D. W. Shin, S. W. Cho, C.-W. Jeon, J. Kim, *Curr. Appl. Phys.* **2020**, *20*, 1237.

[34] M. Stolterfoht, V. M. Le Corre, M. Feuerstein, P. Caprioglio, L. J. A. Koster, D. Neher, *ACS Energy Lett.* **2019**, *4*, 2887.

[35] M. D. Mia, C. H. Swartz, S. Paul, S. Sohal, C. R. Grice, Y. Yan, M. Holtz, J. V. Li, *J. Vac. Sci. Technol. B* **2018**, *36*, 52904.

[36] D. W. deQuilettes, S. M. Vorpahl, S. D. Stranks, H. Nagaoka, G. E. Eperon, M. E. Ziffer, H. J. Snaith, D. S. Ginger, *Science* **2015**, *348*, 683.

[37] M. Stolterfoht, M. Grischek, P. Caprioglio, C. M. Wolff, E. Gutierrez-Partida, F. Peña-Camargo, D. Rothhardt, S. Zhang, M. Raoufi, J. Wolansky, M. Abdi-Jalebi, S. D. Stranks, S. Albrecht, T. Kirchartz, D. Neher, *Adv. Mat.* **2020**, *32*, 2000080.

[38] U. Würfel, D. Neher, A. Spies, S. Albrecht, *Nat. Commun.* **2015**, *6*, 6951.

[39] F. D. Eisner, M. Azzouzi, Z. Fei, X. Hou, T. D. Anthopoulos, T. J. S. Dennis, M. Heeney, J. Nelson, *J. Am. Chem. Soc.* **2019**, *141*, 6362.

[40] M. Bixon, J. Jortner, J. W. Verhoeven, *J. Am. Chem. Soc.* **1994**, *116*, 7349.

[41] VDMA, International Technology Roadmap for Photovoltaic (ITRPV): 2019 Results, https://itrpv.vdma.org/ (assessed: December 2020).

[42] M. G. Moharam, T. K. Gaylord, *J. Opt. Soc. Am.* **1981**, *71*, 811.

[43] P. Lalanne, G. M. Morris, *J. Opt. Soc. Am.* **1996**, *13*, 779.

[44] M. G. Moharam, T. K. Gaylord, *J. Opt. Soc. Am.* **1982**, *72*, 1385.

[45] M. List, T. Sarkar, P. Perkhun, J. Ackermann, C. Luo, U. Würfel, *Nat. Commun.* **2018**, *9*, 3631.